Batteries & Supercaps

Research Article
doi.org/10.1002/batt.202400301

Chemistry
Europe
European Chemical
Societies Publishing

www.batteries-supercaps.org

Dry-Pressed Fabrication of Lithium-Ion Electrodes Over 500 μm Thick

Kedi Hu,[b] William Fu,[b] Alan C. West,*[a] and Daniel A. Steingart*[a]

In stationary storage, thick electrodes can minimize inactive material components to increase energy density and decrease cost, but they face challenges in performance and manufacturability. This work discusses a method to fabricate thick-format lithium-ion electrodes and a model to explore transport constraints for functional thick electrodes. Thick lithium iron phosphate (LFP) electrodes were fabricated using a solvent-free pressing process that adopts methods from alkaline electrode manufacturing for low-cost scale-up. LFP electrodes with thicknesses up to 1 mm and capacities up to ~15 mAh/cm^2 exhibited good rate performance (~98% utilization at C/10, ~95% at C/5, ~76% at C/2). A physics-based LFP half-cell model was developed to aid in characterizing transport within these thick electrodes, revealing opportunities to further improve performance by decreasing tortuosity.

Introduction

Energy storage systems are necessary to bridge intermittency and enable the use of low-cost renewable energy in place of fossil fuels for grid-scale electricity generation. Based on a study by Shaner et al., 12 hours of storage is needed for wind/solar mixes to power the United States' electricity grid with 80% reliability.[1] Lithium-ion batteries (LIBs) are attractive for large-scale storage because they are a mature chemistry with high cycle life and rate capabilities.

Most Li-ion batteries today have been developed for the electric vehicle and consumer electronics industries. Because fast charging is essential in these applications, electrodes are thin, 50 to 100 μm, to expedite the transport of lithium ions (Li +) across the electrode. The three primary form factors of LIBs – pouch, cylindrical, and prismatic cells – employ multiple thin layers of cathode, separator, anode, and current collector, either wound or stacked within the cell body, increasing cell material costs.[2,3] In 2023, the cost of 4 hour battery storage with current Li-ion technologies stands at around $482/kWh at the system level, which is too high for grid-scale adoption of LIBs.[4] Ziegler et al. have shown that for a grid system where wind and solar energy meet 95% of electricity demand, the requisite energy capacity cost stands at < $150/kWh.[5] To decrease the cost of grid storage, a techno-economic study by Ciez and Steingart revealed that increasing electrode thicknesses to 300 μm and

beyond can reduce cell-level costs from $90-$140/kWh to $60–80/kWh.[6]

Traditional slurry-cast electrodes in LIBs are made by dispersing a mix of active material, binder, and carbon black in a solvent – typically N-Methylpyrrolidone (NMP) for the cathode and water for the anode – casting this slurry onto a current collector foil, then evaporating the solvent to leave behind the electrode composite. In thick electrodes, however, solvent processing poses several additional challenges: nonuniformity due to migration of binder and carbon black with the solvent as it evaporates, cracking and delamination of the electrode from the current collector, long drying ovens which incur greater manufacturing costs, and large volumes of NMP, which is toxic and energy-intensive to recover.[7]

In recent years, various processes have been developed to eliminate the use of solvents in electrode manufacturing. Among them, electrostatic spraying and extrusion-based processes are especially attractive because they can be implemented on existing roll-to-roll electrode manufacturing lines.[8–13] The dry extrusion process, developed by Maxwell Technologies and employed by Tesla in recent years, involves a shear-induced binder fibrillation step, typically with a polytetrafluoroethylene (PTFE) binder, to allow for the powder mix to be extruded into a sheet electrode.[10–15] Our process, highlighted in Figure 1, forgoes this fibrillation step, employing a heating and die-pressing process to form a thick, free-standing pressed electrode.

This dry-pressing method is presented as a lab-scale prototype for adopting free-standing electrode manufacturing techniques field-tested and validated in alkaline battery production.[16] Our simple lab-scale pressing method yields
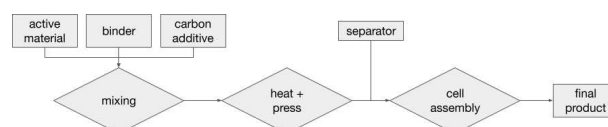
[a] A. C. West, D. A. Steingart
Chemical Engineering, Earth and Environmental Engineering, Columbia Electrochemical Energy Center, Columbia University, 500 West 120th St., New York, NY 10027, USA
E-mail: acw7@columbia.edu
das2277@columbia.edu

[b] K. Hu, W. Fu
Chemical Engineering, Columbia University, 500 West 120th St., New York, NY 10027, USA

Figure 1. Dry Electrode Fabrication Process.

Batteries & Supercaps

Research Article
doi.org/10.1002/batt.202400301

Chemistry
Europe

European Chemical
Societies Publishing

thick, high-capacity (~15 mAh/cm^2) electrodes with good performance (~98% utilization at C/10, ~95% at C/5) at low discharging rates relevant to grid storage. Utilization drops off at higher c-rates (~76% at C/2) but can be addressed through transport optimizations. A Doyle-Fuller-Newman (DFN)-style model is employed to study the transport of Li-ions in the thick pressed electrodes and design constraints for future thick-format cells.[17–20] Fitted to our data, the model reveals that not only is thickness significant in limiting Li$^+$ transport, tortuosities may also be significantly higher in the thick dry-press electrodes than in conventional slurry-cast electrodes. These transport limitations highlight the importance of future research on pore engineering techniques, such as templating with pore formers, that can be implemented on a roll-to-roll or die-press manufacturing line.[7]

Methods

Electrode Fabrication & Characterization

Carbon-coated lithium iron phosphate (LFP; MSE), polyvinylidene difluoride (PVDF; Kynar HSV900), and carbon black (CB; Ketjen 600JD) were hand-milled at a mass ratio of 75:15:10 LFP:PVDF:CB. The MSE LFP is reported to have a particle size distribution of: D10: 0.55 μm, D50: 1.5 μm, D90: 6.0 μm. To create a pellet, 0.1 g–0.15 g of powder was loaded into a 12.7 mm diameter pellet die (MSE), heated in a 270 °C oven for 1 hour, and pressed for 1 minute using a Dake F-10 hydraulic press. A range of pressures from 100–300 psi were used to press electrodes with different thicknesses and gravimetric porosities. Electrodes were massed and thickness measurements taken on a tabletop micrometer (Mituyo) are reported as an average of five values across the electrode. Porosity (ε_{grav}) was calculated gravimetrically from thickness and mass measurements according to Equations (1) and (2),

$$\varepsilon_{grav} = 1 - \nu_{LFP} - \nu_{PVDF} - \nu_{CB} \tag{1}$$

$$\nu_i = \frac{w_i\ m_{pellet}}{\rho_i\ L\ \pi\ r^2} \tag{2}$$

where m, L, and r are the pellet mass, thickness, and radius. The volume fraction of each material (ν_i) is calculated from its mass fraction (w_i) and density (ρ_i). The material densities of LFP, PVDF, CB used for this calculation were 3.6, 2.28, and 1.78 g/cm^2 respectively. A Thermo Scientific Phenom Pure desktop scanning electron microscope (SEM) was used to take images and energy dispersive spectroscopy (EDS) maps of the electrodes.

Slurry-cast electrodes were made by hand-milling the LFP, PVDF, and CB at a mass ratio of 90:5:5 respectively, dispersing the solid mixture in NMP (Sigma-Aldrich) with a 1:2 solid to liquid mass ratio by mixing on a stir plate for two days, and casting onto a 12 μm thick aluminum current collector using a doctor blade with a gap thickness of 200 μm. The solvent was evaporated by heating for 1 hour at 80 °C, then 4 hours at 110 °C in a vacuum oven (Biobase). The dried electrodes were punched into 12.7 mm diameter discs using tabletop disc cutter (MTI). The three electrodes selected for testing have an average areal capacity loading of 0.459 mAh/cm^2. The electrodes were used uncalendered with high porosities (0.81 ± 0.076) to represent thin electrode performance with minimal transport limitations.

Coin Cell Assembly & Cycling

CR2032 coin cells were made inside an argon-filled glovebox (MBRAUN). Before assembly, all electrodes were dried under vacuum overnight at 120 °C. Pellet electrodes were then soaked for a day in 1 mL of liquid electrolyte, 1 M lithium bis(fluorosulfonyl)imide (LiFSI; Gotion) in 1:1 v/v dioxolane (DOL; Sigma-Aldrich)/dimethoxyethane (DME; Sigma-Aldrich). All cells were assembled with 200 μL of liquid electrolyte, a 25 μm thick separator (Celgard 2325), and a pre-cut 0.6 mm thick, 16 mm diameter lithium metal disk (MSE).

Cells were cycled at 25 °C on a Neware battery cycler. All cells were formed using two cycles at a C/40 rate, then underwent rate performance tests using the following cycling protocol: 2 C/10, 2 C/5, 2 C/2. All cells were charged using a constant current (CC) charge followed by a constant voltage (CV) hold with a C/40 cutoff current. All cells were discharged using a constant current.

Theory

A Newman-style physics-based model was developed to produce simulated electrochemical cycling data for a LFP half cell.[17–22] The governing equations and boundary conditions are summarized in Figure 2. A full table of model equations are included in Supplementary Table S1.

Parameter estimation was based on the method of Brady et al.[23,24] Sobol sampling was used to generate parameter sets within a defined parameter space. Experimental data was compared to the model by calculating a residual sum of squares (RSS). Each parameter set maps to an RSS, which are assumed to be normally distributed within the specified parameter range. The fitted parameters are reported using their distributions' average value.

Three thin slurry-cast electrodes were cycled according to the protocol detailed in Methods, and the data were used to fit a pseudo-2D thin electrode model in which particle-scale diffusion is dominant, and the crystal-scale diffusion coefficient (D_{LFP}) is extracted from this model. Because electrode-scale transport is dominant in a thick electrode, a 1D model was used for the thick model. The thick electrode model employs a three-parameter space comprised of tortuosity (τ), electronic conductivity (σ), and reaction constant (k_{rxn}). In our study, the electrolyte diffusion coefficient (D_{LiFSI}) was estimated to be ~1.13×10^{-5} cm^{2}s^{-1} using a measurement by Zhang et al. for a 1 M LiFSI in DME electrolyte and a correction factor for the DOL:DME mixture based on molecular dynamics simulations by Park et al.[25,26] Using a fixed value for D_{LiFSI}, tortuosity was fit to determine an effective diffusion coefficient based on Equation (3). The estimated model parameters are listed in Table 1.

$$D_{eff} = D_{LiFSI}\ \frac{\varepsilon}{\tau} \tag{3}$$

Figure 3 shows how the simulated voltage curves produced from the fitted thick electrode model compare to experimental results at different c-rates. Experimental data was collected in triplicate; the solid lines denote the average voltage curves and the shaded regions represent the standard deviation attained by the replicate experiments. The normalized state-of-discharge (SOD) on the x-axis is calculated for experiments by dividing the capacity by the maximum capacity attained on discharge. In Figure 3, at lower c-rates of C/10 and C/5, the simulations and experiments fit quite closely. At C/2, the experimental data deviates more significantly from the model. In the experimental data, thick electrodes exhibit greater sloping in the voltage curve at higher c-rates.
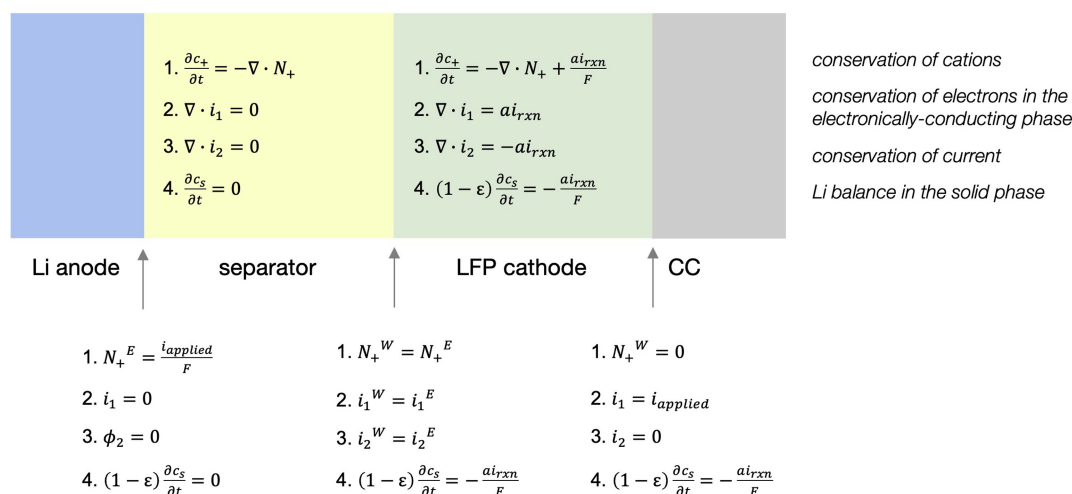
Figure 2. Physics-based model configuration, with governing equations and boundary conditions.

Table 1. List of modeling parameters for the thick electrode 1D model. Experiment parameters for capacity loading, thickness, porosity, and percent accessible active material are averaged properties of the three thick electrodes used to fit the model.

Experiment Parameters		Value
	composition (LFP:PVDF:CB)	75:15:10
Q_{theor}	capacity loading	14.77 ± 0.328 mAh cm^{-2}
x_{max}	thickness	1006.7 ± 25.7 μm
ε	porosity	0.61 ± 0.012
%AAM	percent accessible active material	91.4 ± 2.43 %
$c_{0,\,init}$	initial salt concentration	1 M
Literature & Fitted Parameters		Value
D_{eff}	effective diffusion coefficient of LiFSI in the bulk electrode	8.0×10^{-7} cm^2 s^{-1}
D_{LiFSI}	diffusion coefficient of LiFSI in the electrolyte	1.13×10^{-5} cm^2 s^{-1}
D_{LFP}	diffusion coefficient in LFP solid[c]	3.16×10^{-10} cm^2 s^{-1}
σ	electronic conductivity[c]	2.188 S cm^{-1}
k_{rxn}	reaction constant[c]	1.26×10^{-9} mol$^{0.5}$ s^{-1} cm$^{-0.5}$
$\tau_{electrode}$	electrode tortuosity[c]	8.65
L_{sep}	separator thickness[a]	25 μm
$\tau_{separator}$	separator tortuosity[b]	4.1
$x_{max,c}$	particle diameter	5 μm

[a] Measured. [b] Literature.[25,26,28,29] [c] Extracted from model-experimental comparison.

The open-circuit potential model used in this work is from Srinivasan and Newman's 2004 LFP half-cell model.[19] This model, while thermodynamically consistent, neglects the single-phase region of the LFP reaction at the beginning of discharge.[19,27] Inclusion of the initial single-phase region could improve high-rate fits at low states of discharge in a future model.

In their thin electrode model, Srinivasan and Newman observed a similar phenomenon in which increasing polarization with state of discharge (SOD) produced sloping curves, especially at higher current densities (c-rates). Srinivasan and Newman attributed this increasing polarization to an ohmic effect in which the ohmic drop increases with SOD.[19] For example, if the reaction distribution within the porous electrode is nonuniform, current may travel through longer, less conductive paths towards the end of discharge.[19] Their analysis offers insight into ohmic limitations in the thick dry-pressed electrodes. The sloping that their 62 μm thin electrodes exhibit at C/2, 1 C, and 2 C is akin to the sloping of our thick electrodes at C/10, C/5, and C/2, respectively, which suggests that material heterogeneities from the wide particle size distribution of the MSE LFP and more tortuous electronic pathways within the thick electrode may exacerbate this type of ohmic polarization due to nonuniform reaction distribution.

Results and Discussion

Thin slurry-cast and thick pellet LFP electrodes were assembled into half cells and cycled using a sequential rate performance
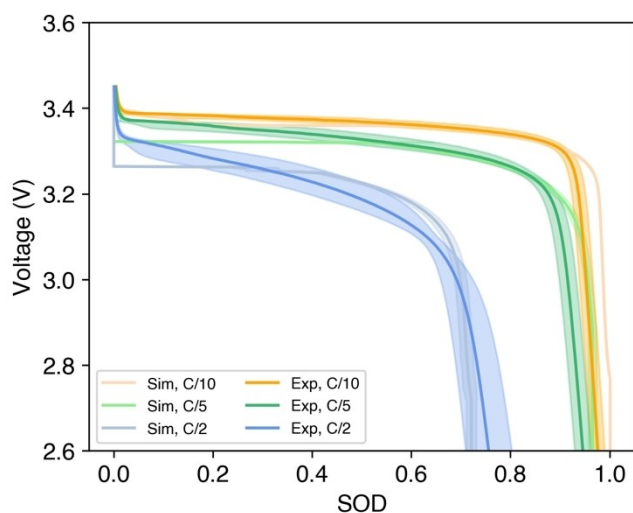
Batteries & Supercaps

Research Article
doi.org/10.1002/batt.202400301

Chemistry
Europe
European Chemical
Societies Publishing

Figure 3. Simulated and experimental voltage curves for the thick pellet electrodes at different c-rates, C/10, C/5, C/2. Solid lines denote the average voltage curves and the shaded regions represent the standard deviation attained by the replicate experiments.

test of 2 C/10 cycles, 2 C/5 cycles, then 2 C/2 cycles. Data for each electrode type was collected in triplicate, and the voltage curves for each cycle of each cell were interpolated to obtain a set of SOD values for a fixed set of voltage values to allow for averaging. SOD was calculated by dividing the experimental capacity by the maximum accessible discharge capacity at a slow (C/40 or C/10) rate. In Figure 4, solid lines denote the average SOD at each value of voltage, and the shaded regions represent the range attained by the replicate experiments. Despite being over an order of magnitude larger in thickness (1000 ± 25 μm vs 70 ± 10 μm) and roughly an order of magnitude larger in capacity (~15 mAh cm^{-2} vs ~1.4 mAh cm^{-2}), the thick pellet electrodes were able to achieve nearly full utilization at C/10 (166 ± 2.3 mAh g^{-1}; 98 ± 1.4% utilization) and at C/5 (161 ± 2.8 mAh g^{-1}; 95 ± 1.7%). At C/2, utilization drops off to 129 ± 7.9 mAh g^{-1} (76 ± 4.7%). In comparison, the thin slurry-cast electrodes obtained 161 ± 3.6 mAh g^{-1} (95 ± 2.1%), 159 ± 7.2 mAh g^{-1} (94 ± 4.2%), and 150 ± 7.8 mAh g^{-1} (88 ± 4.6%) at c-rates of C/10, C/5, and C/2 respectively. Discharge capacity and coulombic efficiency of each thin and thick electrode half cell is reported in Supplementary Figure S1.

At lower c-rates, high utilization in the thick electrodes is attributed to their high porosities (~0.6) which offers both 1)
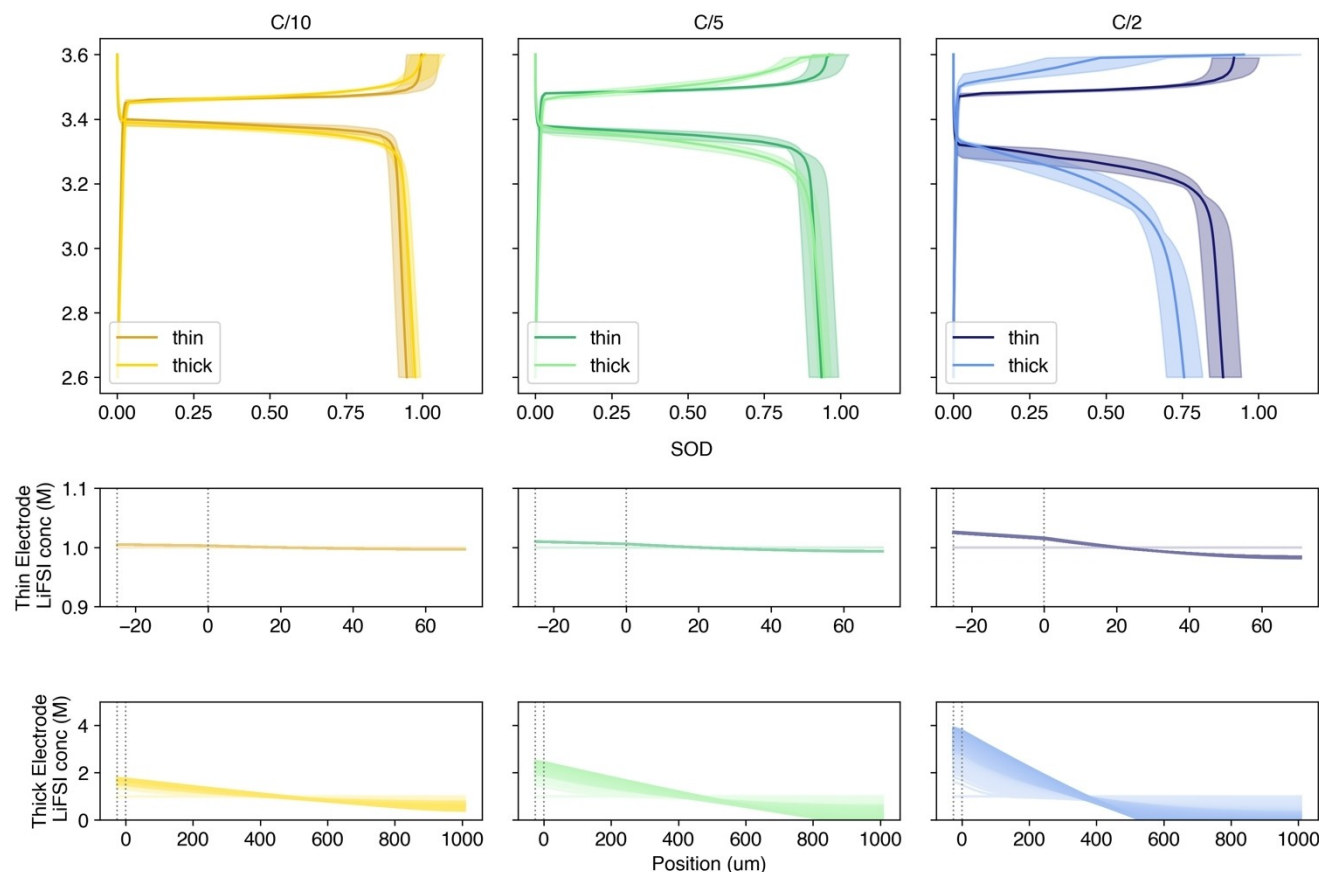

Figure 4. Experimental rate performance for thin slurry-cast electrodes compared to thick 75:15:10 pellet electrodes (1st row). Solid lines denote the average voltage curves and the shaded regions represent the range attained by the replicate experiments. Simulated concentration gradients across thin (2nd row) and thick (3rd row) electrodes where position is the through-thickness position. The portion between the dotted lines (Position = −25 to 0 μm) indicates the separator region, the dotted line at Position = 0 μm is the separator-cathode interface, and the portion to the right of the dotted lines (Position > 0 μm) represents the electrode. For the concentration gradients, light to dark shows increasing time.

more pathways for ion transport and 2) a greater likelihood of less-tortuous ionic pathways. Additionally, a LiFSI electrolyte was used in place of a more conventional lithium hexafluorophosphate ($LiPF_6$) electrolyte to stabilize high current density plating/stripping on the Li metal counter electrode.[30] LiFSI is reported to have higher ionic conductivities and diffusion coefficients (15.2 mS cm^{-1} and 1.47×10^{-5} cm^2 s^{-1} for 1 M LiFSI in DME) than conventional $LiPF_6$ electrolytes (~10 mS cm^{-1} and 2 to 5×10^{-6} cm^2 s^{-1} for 1 M $LiPF_6$ in EC/DEC), which enhance Li$^+$ ion transport through the porous LFP electrode.[25,28,31,32]

At a higher c-rate of C/2, however, utilization drops off more significantly in the thick electrodes (~78% of their C/10 capacity) than in the thin electrodes (~93% of their C/10 capacity). At a higher thickness, steeper Li-ion concentration gradients develop to push lithium ions through the thickness of the electrode (Figure 4). These larger concentration gradients translate to larger concentration overpotentials, which cause the cell to hit a voltage cutoff before the full capacity of the electrode is used. This underutilization is further exacerbated by the larger internal resistance (IR) drop at higher c-rates.

There is also some asymmetry in the charge and discharge rate performance of the thick electrodes. All electrodes were charged using a constant current (CC) at the given c-rate, followed by a constant voltage (CV) hold at the top-of-charge cutoff voltage until the current tapered to a value below the C/40 current. This CCCV procedure allows us to get a sense of the rate performance during charge, without significantly compromising the capacity attained during discharge. The portion of the charging curve before the knee point gives a value for the constant current charge capacity. Because the CCCV charge is combined in one step on the cycler, the constant current portion of charge is extracted in Figure 5 by taking the segment of the charge curve where the current remains within 95% of the initial current value, which is specified by the c-rate and capacity loading of the LFP electrode. For the thick pellet electrodes, while our CC charge and discharge performance are roughly symmetric for C/10 (169 ± 6.9 mAh g^{-1} vs 166 ± 2.3 mAh g^{-1}, charge vs discharge), CC charge performance

drops off relative to CC discharge performance at C/5 (150 ± 6.6 mAh g^{-1} vs 161 ± 2.8 mAh g^{-1}), and even more severely at C/2 (88 ± 27.3 mAh g^{-1} vs 129 ± 7.9 mAh g^{-1}). Krieger and Arnold attribute asymmetry in charge and discharge performance to undercharge: voltage values on charge are closer to the cutoff, so charging steps are more likely to be cut off early.[33] This is especially the case in our two-phase LFP system, where a flat plateau near the top voltage cutoff dominates the voltage curve. Exacerbated by larger overpotentials due to higher internal resistance at higher power (higher c-rates), the cell is more likely to be undercharged using a constant current procedure at C/2.

Overall, the cell drops off in performance at C/2, both on charge and discharge. C-rates as fast as C/2, however, may be less relevant for grid applications in the future, especially since thicker electrodes can deliver higher current densities and therefore higher power at lower c-rates.

Electronic conductivity for the freestanding pellet electrode is considered in two ways: 1) bulk electrode conductivity and 2) electronic connection to current collector. First, compared to conventional slurry-cast electrodes, the freestanding electrode has a much larger conductive carbon mass fraction (10% vs 5%) to promote electronic conductivity within the electrode. Second, the freestanding electrode, while not laminated, still receives current conduction through a SS spacer. Compared to aluminum, SS is less conductive, but would not be limiting electronic conduction with respect to the bulk electrode. The electrode's contact with the SS spacer is maintained by the pressure exerted by the spring in the coin cell. Compared to a laminated current collector, this could result in higher contact resistance, which may result in an overall downward shift of the voltage curves. At higher c-rates (higher currents), this resistive overpotential would be larger based on Ohm's law, resulting in lower apparent capacity given the cutoff voltages.

Figure 6 shows experimental rate capability data for multiple pellet electrodes as a function of porosity. For a given c-rate, simulated capacity and utilization data is weakly dependent on porosity (see Supplementary Figure S1). Therefore, simulated data for $\varepsilon = 0.6$ are selected as representative curves and are shown here.

The simulated data in the green are plotted as a function of accessible active material (AAM), the fraction of active material loaded into the electrode that can be reached by both lithium ions and electrons and participate in the reaction. In Figure 6a, simulated data for Capacity vs C-rate shows that accounting for %AAM allows the model to fit the experimental data well. The simulated lines for %AAM = 80% to 95% capture the performance of the experimental pellet electrodes, which have experimentally determined values of %AAM (94.2%, 90.1%, and 89.9%) calculated by dividing the capacity at C/10 by the theoretical capacity loading of the electrode.

In the Utilization vs C-rate plot (Figure 6b), simulated lines overlap because they are normalized to the C/10 capacity, which scales as %AAM is scaled. We prioritized the fit of utilization at lower c-rates (C/5) for grid storage applications, and experimental C/2 utilization exceeds our model predictions. The model slightly underpredicts utilization because it slightly
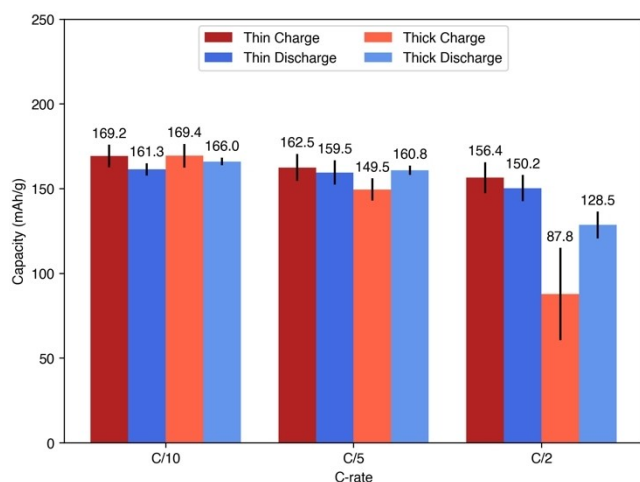

Figure 5. Constant current charge and discharge capacity for thin slurry-cast electrodes and thick 75:15:10 pellet electrodes.

Batteries & Supercaps

Research Article
doi.org/10.1002/batt.202400301

Chemistry Europe
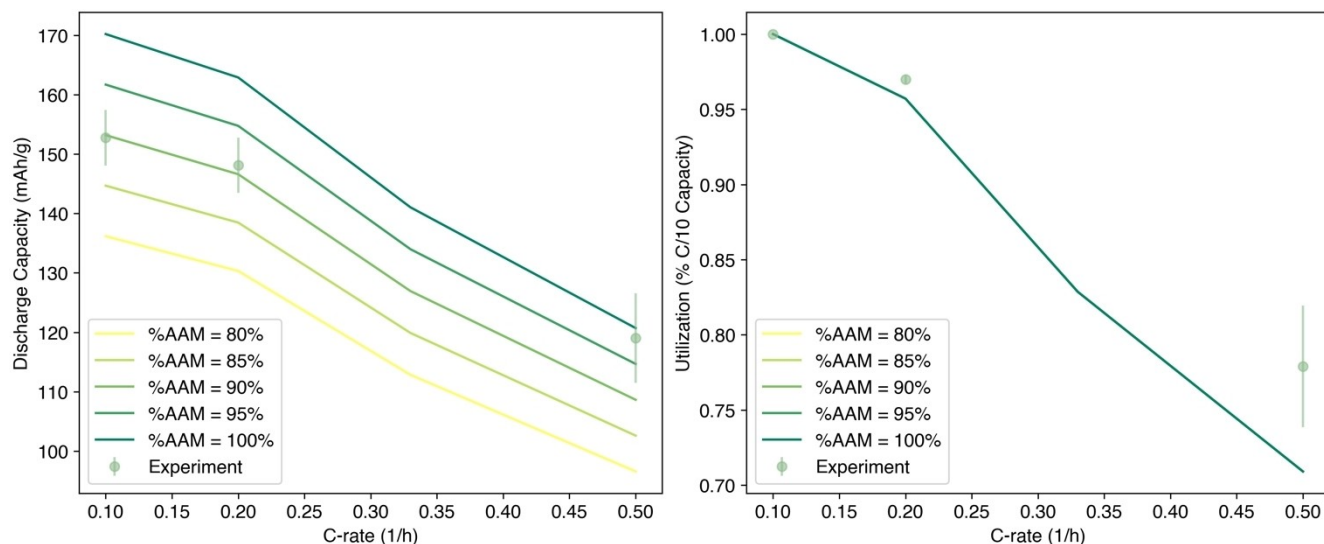European Chemical
Societies Publishing

Figure 6. a) Discharge Capacity and b) Utilization vs C-rate as a function of C-rate, for both simulated and experimentally-tested thick pellet electrodes. Experimental data is plotted with points representing the average values and the shaded region representing the standard deviation. Simulated data at common c-rates (C/10, C/5, C/3, C/2) using a thick electrode with a porosity of 0.6, a tortuosity of 8.65, and an effective diffusion coefficient of 8.0×10^{-7} cm^2 s^{-1} (fitted, see section on Theory), and various percentages of accessible active material are shown in the solid green lines.

overpredicts the capacity attained at C/10 and slightly under-predicts the capacity attained at C/2 (Figure 3). The model was fit to the experimental data by comparing the whole discharge voltage curve, rather than just the end capacity. Furthermore, because each RSS value is calculated from model-experiment residuals given a fixed set of voltages, rather than a fixed set of SOD, the fitted model prioritizes the fit of the plateau over the fit of the ending capacity. The combination of these factors results in a simulated C/2 curve that wavers around the experimental curve, but has slightly larger overpotentials at some SOD, and slightly smaller overpotentials at other SOD. Using a tortuosity that increases with increasing c-rate would improve the fits of the ending capacity but is not physical in this system unless the pellet morphology is rapidly evolving with rate cycling. Future models can explore methods to increase sloping behavior in thick electrode simulations to improve this fit, perhaps through incorporating initial single-phase behavior or surveying physical implementations for increasing ohmic polarization (e.g. particle size distribution).[19]

The model was used to simulate electrode performance for a range of tortuosities and porosities to examine how these diffusion limitations affect utilization (Figure 7). In the simulated data, for a given C-rate, the utilization-tortuosity curve for electrodes of porosities in the range of 0.45–0.7 is very weakly dependent on porosity, as shown in Supplementary Figure S4. Simulated data for the two extremes, $\varepsilon = 0.45$ and $\varepsilon = 0.7$, are shown here.

As expected, simulation results show that utilization decreases with increasing tortuosity. As electrodes become more tortuous, the diffusion and migration pathways for Li-ions increase in length, and greater mass transport overpotentials inhibit full utilization of the electrode.

Thick pellet electrodes were fabricated with varying gravimetric porosities by pressing to different pressures in the pellet
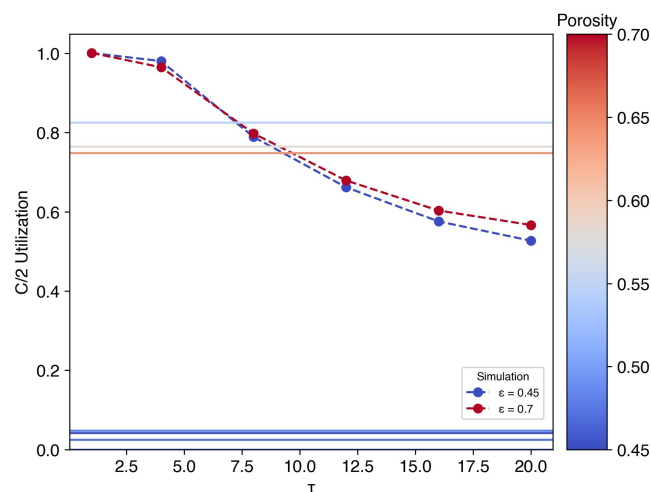

Figure 7. C/2 Utilization as a function of tortuosity. The simulated curve is constructed based on electrodes with porosities of 0.6 and tortuosities ranging from 4 to 20. The bulk electrolyte diffusion coefficient was fixed at 1.13×10^{-5} cm^2 s^{-1}. Experimental data for thick electrodes fabricated with varying gravimetric porosities are plotted as horizontal lines.

die. In Figure 7, experimental data is plotted as horizontal lines because the tortuosities of the electrodes were not experimentally determined. Impedance measurements on blocking electrodes or polarization-interrupt methods[29,34–38] may be used to determine a tortuosity experimentally, but were not employed for the pellets shown in the figure as they cannot withstand repeated assembly and disassembly. Theoretical estimations of tortuosity primarily revolve around variations of the Bruggeman relationship, $\tau = \varepsilon^{-0.5}$. If the experimental data in Figure 7 were to be plotted with tortuosities according to the Bruggeman relationship, they would have tortuosities of 1.28 ± 0.013 and deviate significantly from the simulated tortuosity of 8.65 (Supplementary Figure S5). Other studies have also shown that

the Bruggeman relationship underpredicts tortuosity for a range of materials, especially for electrodes with high binder fraction.[38,39] The intersection of an experimental line with the simulated curve gives an estimate of tortuosity, ranging from 8 to 10 for the top three lines (electrodes with $\varepsilon_{grav} > 0.55$). For a more accurate estimate of a specific electrode's tortuosity, the model could be fit to the individual electrode's data, based on variation in accessible active material loading and porosity. The modeled tortuosity of 8.65 reported is fit to three thick electrodes with $\varepsilon_{grav} > 0.55$ and uses probability density functions to calculate the most likely value of tortuosity that would fit all three of the electrodes.

While the tortuosity values of 8 to 10 seem high, Bernard et al. showed that tortuosity has a dependence on the binder fraction of the electrode, reporting modeled tortuosity estimates of 10 to 20 for electrodes with a binder fraction of 15 wt%.[38] The pellet electrodes in this study use 15 wt% PVDF, but are slightly higher in porosity (~0.6) compared to Bernard et al.'s electrodes (0.4–0.5), so a slightly lower tortuosity range of 8 to 10 is reasonable.[38] Additionally, Bernard et al.'s estimates were based on a conventional slurry-casting method, and further variation in tortuosity may arise from the pellet-pressing process. For example, pellets are pressed such that the pressing plane is oriented orthogonally to the direction of ionic transport in the cell. If there is flattening and elongation of particles in the electrode composite, as later SEM images suggest (Figure 8b), this would exacerbate the through-thickness tortuosity. Further advancements in pore engineering, such as templating, additive/subtractive manufacturing, and phase inversion techniques, to decrease the through-thickness tortuosity will improve Li-ion diffusion, especially at higher c-rates, making these thick electrodes more viable for high-power (e.g. electric vehicle) applications.[7,40]

Figure 7 shows that while tortuosity can account for some variation in discharge capacity and utilization, even an unrealistically large range of tortuosities (1 to 20) cannot explain the poor performance of the darker blue lines, pellet electrodes with lower gravimetric porosity ($\varepsilon_{grav} < 0.55$). While these porosities are still high compared to conventional electrodes ($\varepsilon \sim 0.3$), the gravimetric porosity measurement does not account for closed pores, so the accessible porosity in these pellet electrodes could actually be lower. Nonuniform wetting in the thick electrodes could further exacerbate underutilization by limiting reaction sites where lithium ions can access the active material. Simply accounting for a smaller fraction of accessible active material, however, is not enough to explain the extreme drop off in capacity moving from C/10 to C/5 (Supplementary Figure S3). This suggests that microstructure changes that evolve with cycling, such as pore occlusion which occurs over time through volume expansion and formation of passivating layers of CEI, or loss of wetting through electrolyte oxidation and local electrolyte drying may be worth exploring in future work.

Cross-sectional SEM images begin to suggest that there are microstructure differences in electrodes with the same amount of active material but pressed to different thicknesses. Compared to the thicker electrode in Figure 8a, the lower thickness electrode in Figure 8b shows carbon black chunks elongated
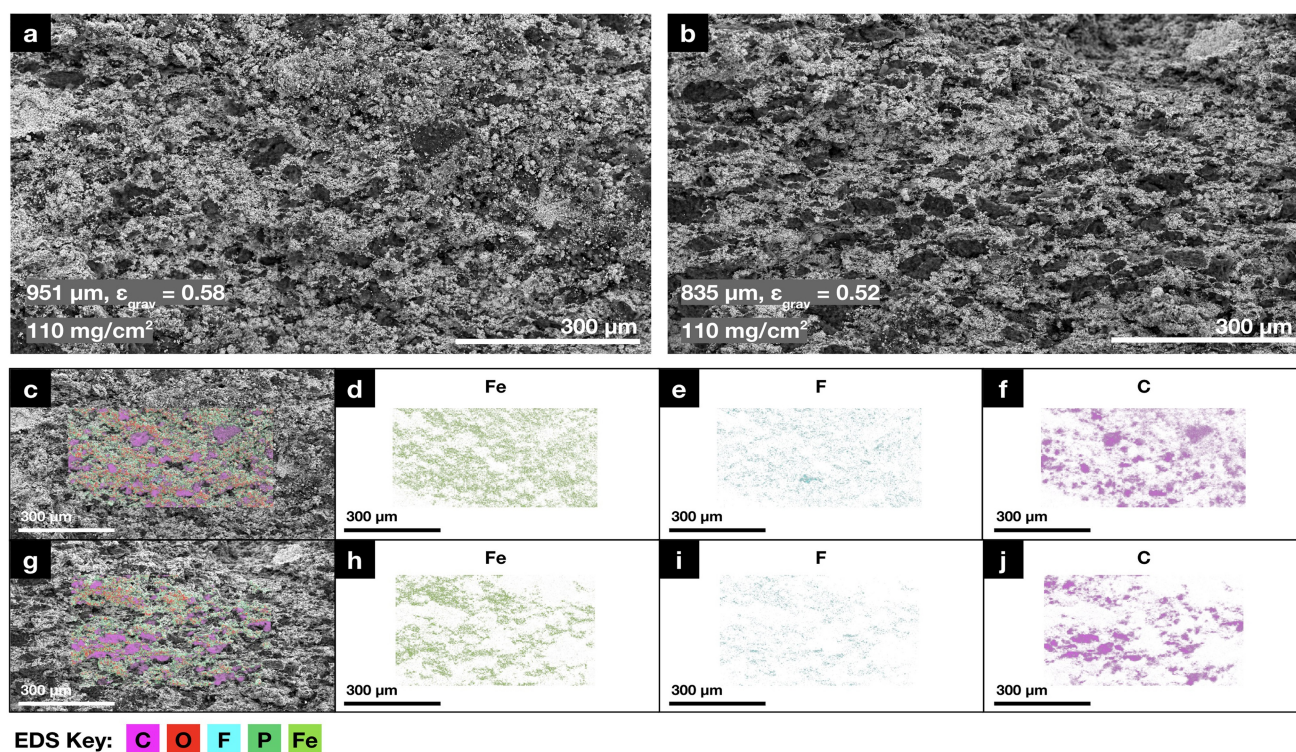

Figure 8. SEM images and EDS maps of pellet electrode cross-sections. The pellets are the same mass loading, pressed to different thicknesses using different pressures. a, c–f) are images of a higher thickness electrode and b, g–j) are images of a lower thickness electrode. The images are oriented such that the pressing plane is along the horizontal edge.

parallel to the pressing plane. Energy dispersive spectroscopy (EDS) was used to map elements throughout the electrode. In Figure 8c–j, Fe corresponds to LFP distribution, F corresponds to PVDF distribution, and C corresponds to carbon black distribution. Overall, the LFP, binder, and carbon black appear to be evenly distributed throughout the electrodes.

Conclusions

We demonstrated a lab-scale prototype process for producing dry-pressed electrodes similar to those used in low-cost alkaline battery manufacturing. We fabricated free-standing, 1 mm thick LFP cathodes with high capacity loadings ~15 mAh cm^{-2}. In half cell configuration, these electrodes were able to achieve high utilization at c-rates relevant to baseload stationary storage, ~98% at C/10 and ~95% at C/5.

A physics-based model was developed to study transport in these electrodes, revealing that not only is thickness a dominant factor in limiting Li$^+$ transport, large tortuosities further exacerbate the underutilization of the active material. Furthermore, when attempting to decrease porosities to below $\varepsilon_{grav} = 0.55$, differences in electrode microstructure exacerbate underutilization of the active material, even at low c-rates of C/10 and C/5. These limitations highlight the need to reduce binder fraction and develop pore engineering techniques able to be implemented on roll-to-roll or die-press manufacturing lines, to simultaneously reduce porosity and tortuosity while retaining high active material utilization. Future studies exploring material distribution and microstructure evolution in the thick electrodes could be valuable in designing thick electrodes with not only high capacity, but also long cycle life.

List of Symbols

%	AAM percent accessible active material
σ	electronic conductivity, S cm^{-1}
a	specific surface area, cm^2 cm^{-3}
c_s	concentration of Li in the solid iron phosphate, mol cm^{-3}
$c_{s, max}$	maximum concentration of Li in the iron phosphate lattice, mol cm^{-3}
c_0, c_+	concentration of Li$^+$ in the electrolyte, mol cm^{-3}
$c_{0, init}$	initial electrolyte concentration, mol cm^{-3}
D_{eff}	effective diffusion coefficient of Li$^+$ in the bulk electrode, cm^2 s^{-1}
$D_0,$	D_{LiFSI} diffusion coefficient of Li$^+$ in the electrolyte, cm^2 s^{-1}
$D_c,$	D_{LFP} diffusion coefficient of Li in LFP solid, cm^2 s^{-1}
ε	porosity
ε_{grav}	gravimetric porosity
F	Faraday's constant, 96485 C mol^{-1}
$i_{applied}$	applied current, mA cm^{-2}
i_{rxn}	reaction current, mA cm^{-2}
i_1	current through the solid, mA cm^{-2}
i_2	current through the electrolyte, mA cm^{-2}
k_{rxn}	reaction constant, mol$^{0.5}$ s^{-1} cm$^{-0.5}$
N_+	flux of lithium ions, mol Li$^+$ cm^{-2} s^{-1}
v_i	volume fraction of material i
Φ_1	solid potential, V
Φ_2	electrolyte potential, V
Q_{theor}	capacity loading, mAh/g
ρ_i	density of material i, g cm^{-3}
τ	tortuosity
w_i	mass fraction of material i
x_{max}	thickness, cm
$x_{max,c}$	particle diameter, cm

Conflict of Interests

The authors declare no conflict of interest.

Data Availability Statement

The data that support the findings of this study are available from the corresponding author upon reasonable request.

[1] M. R. Shaner, S. J. Davis, N. S. Lewis, K. Caldeira, *Energy Environ. Sci.* **2018**, *11*, 914–925.
[2] O. Schmidt, A. Hawkes, A. Gambhir, *Nat. Energy* **2017**, *2*, 1–8.
[3] J. W. Choi, D. Aurbach, *Nat. Rev. Mater.* **2016**, *1*, 1–16.
[4] W. Cole, A. Karmakar, *Cost Projections for Utility-Scale Battery Storage: 2023 Update, National Renewable Energy Laboratory*, can be found under https://www.nrel.gov/docs/fy23osti/85332.pdf, **2023**, (accessed: January 18, 2024).
[5] M. S. Ziegler, J. M. Mueller, G. D. Pereira, J. Song, M. Ferrara, Y.-M. Chiang, J. E. Trancik, *Joule* **2019**, *3*, 2134–2153.
[6] R. E. Ciez, D. Steingart, *Joule* **2020**, *4*, 597–614.
[7] A. M. Boyce, D. J. Cumming, C. Huang, S. P. Zankowski, P. S. Grant, D. J. L. Brett, P. R. Shearing, *ACS Nano* **2021**, *15*, 18624–18632.
[8] B. Ludwig, Z. Zheng, W. Shou, Y. Wang, H. Pan, *Sci. Rep.* **2016**, *6*, 23150.
[9] G. Schälicke, I. Landwehr, A. Dinter, K.-H. Pettinger, W. Haselrieder, A. Kwade, *Energy Technol.* **2020**, *8*, 1900309.
[10] B. Zou, L. Zhong, P. Mitchell, X. Xi (Maxwell Technologies, Inc.), US 2006/0137158 A1, **2006**.
[11] P. Mitchell, X. Xi, L. Zhong, B. Zou (Maxwell Technologies, Inc.), US 2007/012269 A1, **2007**.
[12] P. Mitchell, L. Zhong, X. Xi (Maxwell Technologies, Inc.), US 7342770B2, **2008**.
[13] L. Zhong, US 9236599B2, **2016**.
[14] W. Yao, M. Chouchane, W. Li, S. Bai, Z. Liu, L. Li, A. X. Chen, B. Sayahpour, R. Shimizu, G. Raghavendran, M. A. Schroeder, Y.-T. Chen, D. H. S. Tan, B.

Batteries & Supercaps

Research Article
doi.org/10.1002/batt.202400301

Chemistry Europe
European Chemical
Societies Publishing

Sreenarayanan, C. K. Waters, A. Sichler, B. Gould, D. J. Kountz, D. J. Lipomi, M. Zhang, Y. S. Meng, *Energy Environ. Sci.* **2023**, *16*, 1620–1630.

[15] M. Chouchane, W. Yao, A. Cronk, M. Zhang, Y. S. Meng, *ACS Energy Lett.* **2024**, *9*, 1480–1486.

[16] R. F. Scarr, J. C. Hunter, P. J. Slezak, in *Handbook of Batteries, Third Edition* (Eds.: D. Linden, T. B. Reddy), McGraw-Hill **2002**, 10.1–10.32.

[17] M. Doyle, T. F. Fuller, J. Newman, *J. Electrochem. Soc.* **1993**, *140*, 1526.

[18] T. F. Fuller, M. Doyle, J. Newman, *J. Electrochem. Soc.* **1994**, *141*, 1.

[19] V. Srinivasan, J. Newman, *J. Electrochem. Soc.* **2004**, *151*, A1517.

[20] V. Srinivasan, J. Newman, *J. Electrochem. Soc.* **2004**, *151*, A1530.

[21] J. S. Newman, *Electrochemical Systems*, Prentice-Hall, Englewood Cliffs, NJ, **1973**, pp. 171–177, 217–235, 414–425.

[22] A. C. West, *Electrochemistry and Electrochemical Engineering: An Introduction*, Alan C. West, New York, **2012**, pp. 50–53, 80–82, 93, 107–115.

[23] N. W. Brady, C. A. Gould, A. C. West, *J. Electrochem. Soc.* **2020**, *167*, 013501.

[24] Z. Hui, K. S. Mayilvahanan, Y. Yang, A. C. West, *J. Electrochem. Soc.* **2020**, *167*, 100542.

[25] P. Zhang, H. Jin, T. Wang, M. Wang, *Electrochim. Acta* **2018**, *277*, 116–126.

[26] C. Park, M. Kanduč, R. Chudoba, A. Ronneburg, S. Risse, M. Ballauff, J. Dzubiella, *J. Power Sources* **2018**, *373*, 70–78.

[27] A. M. Yao, V. Viswanathan, *J. Phys. Chem. Lett.* **2024**, *15*, 1143–1151.

[28] A. A. Wang, S. E. J. O'Kane, F. Brosa Planella, J. Le Houx, K. O'Regan, M. Zyskin, J. Edge, C. W. Monroe, S. J. Cooper, D. A. Howey, E. Kendrick, J. M. Foster, *Prog. Energy Combust. Sci.* **2022**, *4*, 032004.

[29] J. Landesfeind, J. Hattendorff, A. Ehrl, W. A. Wall, H. A. Gasteiger, *J. Electrochem. Soc.* **2016**, *163*, A1373.

[30] J. Qian, W. A. Henderson, W. Xu, P. Bhattacharya, M. Engelhard, O. Borodin, J.-G. Zhang, *Nat. Commun.* **2015**, *6*, 6362.

[31] L. O. Valøen, J. N. Reimers, *J. Electrochem. Soc.* **2005**, *152*, A882.

[32] T. Takekawa, K. Kamiguchi, H. Imai, M. Hatano, *ECS Trans.* **2015**, *64*, 11.

[33] E. M. Krieger, C. B. Arnold, *J. Power Sources* **2012**, *210*, 286–291.

[34] N. Ogihara, S. Kawauchi, C. Okuda, Y. Itou, Y. Takeuchi, Y. Ukyo, *J. Electrochem. Soc.* **2012**, *159*, A1034.

[35] M. M. Forouzan, M. Wray, L. Robertson, D. R. Wheeler, *J. Electrochem. Soc.* **2017**, *164*, A3117.

[36] F. Pouraghajan, H. Knight, M. Wray, B. Mazzeo, R. Subbaraman, J. Christensen, D. Wheeler, *J. Electrochem. Soc.* **2018**, *165*, A2644.

[37] I. V. Thorat, D. E. Stephenson, N. A. Zacharias, K. Zaghib, J. N. Harb, D. R. Wheeler, *J. Power Sources* **2009**, *188*, 592–600.

[38] J. C. Bernard, J. C. Hestenes, K. S. Mayilvahanan, L. E. Marbella, A. C. West, *J. Electrochem. Soc.* **2023**, *170*, 030518.

[39] K. S. Mayilvahanan, Z. Hui, K. Hu, J. Kuang, A. H. McCarthy, J. Bernard, L. Wang, K. J. Takeuchi, A. C. Marschilok, E. S. Takeuchi, A. C. West, *J. Electrochem. Soc.* **2021**, *168*, 070537.

[40] J. Wu, Z. Ju, X. Zhang, C. Quilty, K. J. Takeuchi, D. C. Bock, A. C. Marschilok, E. S. Takeuchi, G. Yu, *ACS Nano* **2021**, *15*, 19109–19118.